JOURNAL OF PROPULSION AND POWER
Vol. 23, No. 1, January–February 2007

PIV Study of Wake–Rotor Interactions in a Transonic Compressor at Various Operating Conditions

Jordi Estevadeordal*
Innovative Scientific Solutions, Inc., Dayton, Ohio 45440
and
Steven E. Gorrell† and William W. Copenhaver‡
U.S. Air Force Research Laboratory, Wright–Patterson Air Force Base, Ohio 45433

DOI: 10.2514/1.17452

Details of the unsteady flowfield between an upstream wake generator and a downstream rotor that are closely spaced in a transonic compressor are studied at various operating conditions using particle-image velocimetry. Flow-visualization images and particle-image velocimetry data facilitate analysis of the details of shed vortices, wake motion, and wake–shock interaction phenomena. Such analysis not only aids the understanding of the effect of blade-row interactions on compressor performance but also allows verification of time-accurate CFD codes that are used to characterize transonic compressors. As the operating point changes from choke to stall and the rotor-bow shock moves upstream, distinct vortex-shedding patterns are observed that affect the wake deviation and rotor incidence. With close spacing between the wake generator and the rotor, vortex shedding from the wake generator and the passage of the rotor-bow shock are strongly synchronized and blade-passage "phase-locked" measurements are possible. The resulting multiple images of the flow corresponding to any blade position are averaged to yield vortex and rotor-bow-shock locations at various back pressures. Using various postprocessing methods, specific shed vortices and wake topological features are isolated and details of the wake–shock interaction are captured.

Introduction

BLADE-ROW–WAKE interactions are a significant source of unsteady flow in modern advanced high-performance turbomachines because their design incorporates closely spaced and heavily loaded blade rows to increase thrust/weight. Frequently observed unsteady phenomena such as the interactions of a shock with a vortex and a shock with a blade surface produce nonuniformities and irregular flow patterns that influence compressor performance and result in blade-row vibrations and high-cycle fatigue. A better understanding of these phenomena will aid the design of compressors with improved performance.

The majority of design tools currently in use do not explicitly account for unsteady flows. Multistage axisymmetric models assume that the incoming flow to a blade row is a mixed-out average of the flow exiting the preceding blade row and that potential effects between blade rows are negligible. These models employ empirical correlations based on engine-company design experience to account for the effects of unsteady flow. Another method is based on steady Navier–Stokes analysis, with unsteady interactions between blade rows being modeled as "deterministic stresses" [1]. Its accuracy is dependent on the models used to account for the effects of the unsteady-flow environment on the average-passage flowfield. Time-accurate CFD codes are now used to simulate compressor operation and to investigate complex unsteady-flow phenomena [2,3]. Experimental results that reveal unsteady-flow effects are crucial for validating these design tools and for providing additional understanding of the physical phenomena and interaction processes involved in turbomachinery flows that are associated with closely spaced and heavily loaded compressor stages.

Use of the planar nonintrusive measurement technique particle-image velocimetry (PIV) [4] for complex geometries and unsteady applications has allowed researchers to make accurate measurements of instantaneous and averaged turbomachinery velocity fields [3,5–11]. In the present investigation a system that was developed for obtaining high-resolution velocity data from an axial-flow transonic compressor [12] (Fig. 1) was used to study blade-row interactions at various operation conditions.

The PIV system consists of two Nd:YAG lasers; transmitting and receiving optics; and seeding, synchronization, and camera hardware [6]. The remotely monitored and controlled system allows identification and investigation of the interaction and synchronization of the shed wake and rotor-blade bow shock.

The instantaneous nature of the PIV technique allows for the capture of the instantaneous unsteadiness that is typical of turbomachinery flows, and statistical characterization of the flow is possible through the use of averaging techniques.

Stage-Matching-Investigation Rig

The stage-matching-investigation (SMI) rig is a high-speed highly loaded compressor that consists of three blade rows: a wake generator (WG), a rotor, and a stator (Fig. 2). The rig was designed to permit the WG-to-rotor axial spacing to be set to three values, "close," "mid," and "far" [13], as shown in Fig. 2. The mean spacings that are normalized by the WG chord are given in Table 1.

The WGs were designed to produce a pressure loss typically found in modern-technology highly loaded low-aspect-ratio fan and compressor embedded front stages. To simplify the experiment the WGs were designed to be uncambered airfoils that do not turn the flow. Measurements of stator wakes from rig tests were used as the design target [14]. In general, these wakes are turbulent and do not decay so rapidly as wakes from high-aspect-ratio stages with lower loading. For simplicity and for isolating the effects of various wake parameters, a two-dimensional representation of the wake was desired.

The WG airfoils have a small leading-edge (LE) radius, with a relatively blunt trailing-edge (TE) radius. In the design process this produced the optimum combination of profile and base drag for

Received 29 April 2005; revision received 31 July 2006; accepted for publication 25 August 2006.

*Research Engineer. Associate Fellow AIAA.
†Senior Aerospace Engineer, Compressor Aerodynamics Research Laboratory (CARL), Propulsion Directorate. Associate Fellow AIAA.
‡Principal Scientist, Turbine Engine Division, Propulsion Directorate. Associate Fellow AIAA.

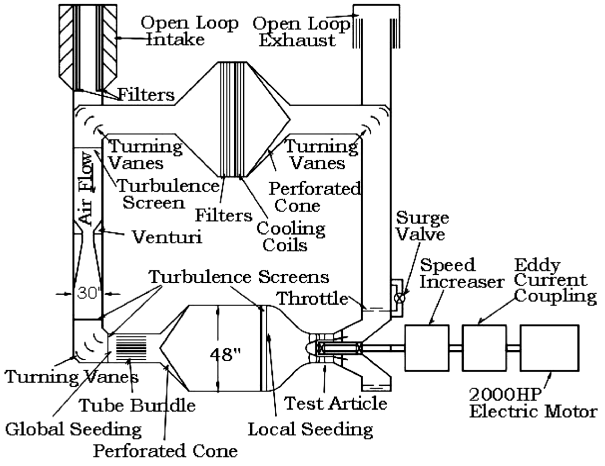

Fig. 1 Flowpath of the 2000-hp Compressor Aerodynamic Research Laboratory facility.

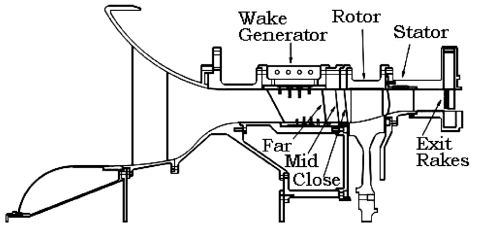

Fig. 2 SMI rig cross section in its general configuration.

matching the desired highly loaded stator wake. To help maintain a constant spanwise total-pressure-loss profile, the solidity of the WGs was held constant from hub to tip, which results in a tapered airfoil chord along the radius. The TE was swept to allow a constant nondimensional mixing length from hub to tip. The clearance was zero at the hub and at the tip.

A compressor map of the overall stage pressure ratio for the 24-WG configuration at close spacing is shown in Fig. 3 (throttle settings: 000, open throttle/choke; 114, peak efficiency; and 140, near stall). A summary of the aerodynamic design parameters is given in Table 2. The present PIV study contains data from measurements made from the 24-WG blade count at "close" spacing at various points on the map. The axial Mach number through the WGs at 75% span was determined to be 0.57; the Reynolds number based on WG TE thickness was 5.78×10^4. The natural nondimensional vortex-shedding frequency (Strouhal number) [15] for an isolated WG airfoil based on the TE thickness is $\sim$0.2.

Particle-Image Velocimetry System

A PIV system that was developed for turbomachinery investigations was employed [6]. Figure 4 contains schematic diagrams of the optical system. Two lasers (Nd:YAG, 532 nm) are employed for double-instantaneous marking of the seed particles in the flowfield. The beams are combined and directed through sheet-forming optics and illuminate the test section with a two-dimensional plane of thickness that is $\sim$1 mm. The scattering from the seed particles is recorded on a cross-correlation CCD camera with 1008 $\times$ 1018 pixels (model Megaplus ES1.0); this camera is capable of acquiring double exposures at 15 Hz. The camera repetition rate was

Table 1 Wake-generator axial spacing (normalized by the local WG chord)

Spacing	x/c, mean	x/c, hub	x/c, tip
Close	0.13	0.10	0.14
Mid	0.26	0.26	0.26
Far	0.55	0.60	0.52

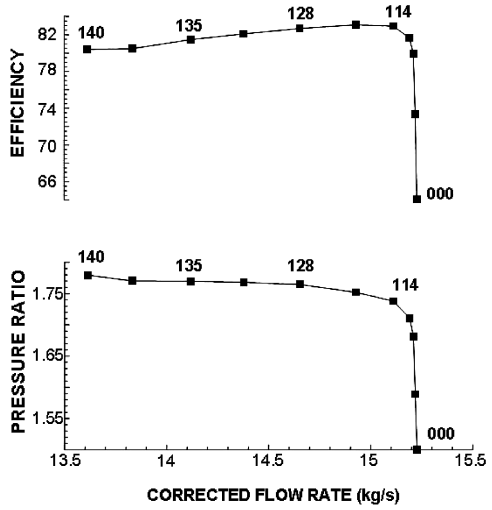

Fig. 3 Overall stage pressure ratio for 24-WG close-spacing configuration.

set at 10 Hz for synchronization with the laser repetition rate. The power for the laser-sheet illumination was $\sim$20 mJ/pulse. A 105-mm Nikon lens set at an f-stop of 5.6 was used. For the present experiments the magnification was 27.4 pixels/mm, which corresponds to an object width of 36.8 mm. The time delay between the two frames of the double exposure was typically 1.25 μs. These settings provided sufficient resolution and accuracy.

The laser-sheet delivery system consists of a probe inserted into an enlarged WG, light-sheet-forming optics, prisms, and probe holders. The outside diameter of the probe is 12.7 mm. To minimize perturbations the modified WG was located at the second WG below the WG that was centered at the receiving window. The optical path from the laser room to the compressor test rig was $\sim$8 m and was covered and isolated from floor vibrations. Figure 4 also contains schematic diagrams of the path for the laser system and the optical probe.

The combined beam entered the SMI case perpendicularly through the center of the WG optical probe. The beam was then turned 90 deg inside the WG by a prism and directed to a spherical lens and a cylindrical lens to form a laser sheet. The laser sheet was turned 90 deg by a prism at the tip of the probe and exited the probe approximately normal to the spanwise (radial) direction. The spanwise location of the laser sheet (Fig. 5) at the window could be changed by rotating the probe. The figure shows two laser-sheet spanwise locations for the 24-WG configuration with respect to the blade clockings, WGs, and 75 and 90% circumferences; blade LE locations are shown at 20-μs intervals with lighter lines. The WG centered at the viewing window (marked by two small lines outward) is at 22.5 deg, and thicker portions of the laser sheets denote PIV

Table 2 SMI aerodynamic design parameters

Parameter	Rotor	Stator
Number of airfoils	33	49
Aspect ratio, average	0.961	0.892
Inlet hub/tip ratio	0.750	0.816
Flow (annulus area), kg/(s $\cdot$ m^{-2})	195.04	——
Flow (frontal area), kg/(s $\cdot$ m^{-2})	85.34	——
Flow rate, kg/s	15.63	——
Tip speed (corrected), m/s	341.6	——
M_{rel} LE hub	0.963	0.82
M_{rel} LE tip	1.191	0.69
Pressure ratio (rotor)	1.88	——
Pressure ratio (stage)	——	1.84
Diffusion factor (hub)	0.545	0.502
Diffusion factor (tip)	0.530	0.491
LE tip diameter, m	0.48260	0.48260
LE hub diameter, m	0.36195	0.39375
WG counts: 24, 40	——	——

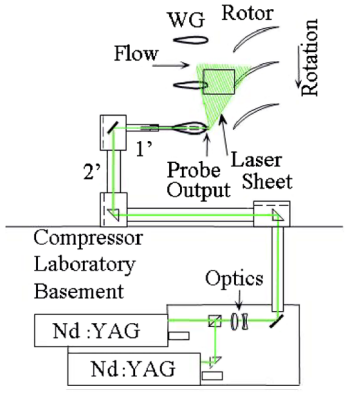

a) Optical path

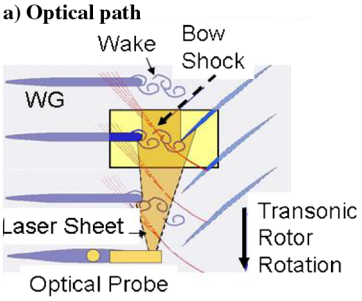

b) Flow features (drawn to scale) showing PIV delivery and receiving optics

Fig. 4 Schematic diagrams of the PIV system.

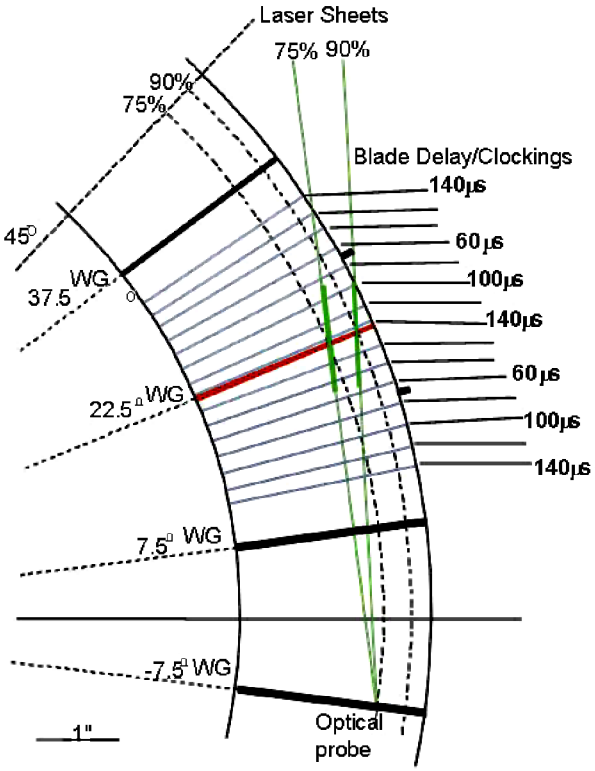

Fig. 5 Laser-sheet spanwise locations for the 24-WG configuration.

image locations. The shape of the laser sheet (thickness, width, and focal distance) could be altered through various combinations of the spherical-lens focal length, the cylindrical-lens diameter, and the distance between them inside the WG as well as through external optics (a spherical lens) located in the laser path. As shown in Fig. 5, the laser sheet was inclined and not at a constant radius. The magnitude of inclination varies depending on the desired spanwise location at the WG TE. Comparison with three-dimensional CFD results can be accomplished in a straightforward manner, requiring interpolation of only the numerical solution to a grid that matches the inclination of the PIV laser sheet. Comparisons have shown that, with the grid densities required to obtain an accurate CFD simulation, an interpolation to a grid that matches the laser-sheet inclination is straightforward [3], and PIV data and unsteady CFD results can be readily compared.

Accurate positioning of the camera was accomplished using a remotely controlled translation stage. The viewing window had the same curvature as the rotor housing (inner housing radius of 241.3 mm), was made of chemically strengthened glass, and was 2 mm thick. Ray-tracing analysis was performed assuming monochromatic laser-sheet (green, 532 nm) glass with an index of refraction of 1.5 (at 20°C), a window with parallel sides, and small angles of incidence and refraction (paraxial approximation) [16]. Comparison of exposures with and without the window was also performed. The results revealed that a negligible magnification of $\sim$0.3% occurs in the vertical direction (affecting the v component) for the present setup. If experiments were conducted with thicker and more curved windows, severe distortion would occur.

The rotor one-per-revolution signal was used for triggering the synchronization system. A digital pulse generator (Stanford DG535) and a camera interface were used. Programming and operation of the camera frame-grabber (National Instruments PCI-1424) and the delay generator were accomplished using drivers that were written especially for the National Instruments LabWindows/CVI development language; this facilitated integration with the PIV analysis software, which is also written in this environment [17].

The seed material employed in previous experiments [6] was submicron-size smoke particles that were generated from a smoke generator using a glycerin and water mixture. During its use in the compressor facility, the seeding system produced sufficient seed when the particles were introduced at the end of the settling chamber, before the contraction, and at the height of the receiving window (Fig. 1). These particles were also preferred for seeding transonic environments because small-size particles with specific gravity similar to that of the air minimize particle lag, including that which occurs when crossing a shock [4]. A pipe extending to the window height was typically inserted into the plenum. The end of the pipe is perforated with holes of increasing diameter toward its end, with a honeycomb and screen for optimal mixing, uniformity, and spreading of seed. Calculations based on flow speed at the beginning of the contraction (the area of maximum diameter and minimum speed), distance from the test area, pipe diameter, and mixing were performed to confirm that the seeding system exerted negligible perturbation on the flow.

Once the PIV images have been captured and digitized, the velocity field was obtained using cross-correlation techniques over interrogation domains of the images and PIV software [4,17]. The dimensions of the interrogation domains were dependent on particle density, estimated local velocity gradients, particle-image size, and desired spatial resolution. The peak of the correlation map corresponds to the average velocity displacement within the interrogation spot. An intensity-weighted peak-searching routine was used to determine the location of the peak to subpixel accuracy. Domain-shifting techniques for minimizing in-plane loss of pairs and correlation–multiplication techniques [18] are used to produce correlation maps with lower noise. Zero padding was also employed for added accuracy [4]. The software includes a grid feature that allows selection of the image areas to be processed, which permits removal of solid regions such as rotor blades and WGs as well as shadows from the processing areas. This feature also provides a choice of various correlation engines and correlation peak locators and incorporates recursive estimation of the velocity field through a multipass algorithm for increased resolution [18]. To maintain high accuracy, two and three passes were performed with interrogation cells overlapping 75%; this yielded a grid resolution of 16 and 8 pixels (corresponding to 0.58 and 0.29 mm), respectively. Overlapping of interrogation domains yields more vectors. The

overlapping is not merely interpolation because it includes new particles in every subregion.

In the present study analyses were performed using averages from the PIV velocity fields. PIV is instantaneous in nature but cannot provide temporal evolution of the flowfield because of the relatively slow repetition rate of the lasers that are suitable for this type of PIV application. The approach taken in this study was based on ensemble (or phase) averaging [19] because of the natural phase locking that is provided by the rotor-blade potential field. Then the temporal evolution could also be inferred from the phase information. The experiments provided a sufficient number of realizations [20,21] (>50) for each average velocity-field calculation. The calculation of turbulence characteristics would benefit from higher numbers, but this was not an objective of the present study. In this study the averaged data is presented using the median. The median is less affected by "outliers" than the mean ("robust statistic") [22], does not require that data be normally distributed, and offers a smooth representation of the ensemble-average velocity fields. It is also an actual member of the data set (for an odd number of samples). The median has also been found to be advantageous when a lower number of realizations is available; the median is further enhanced in studies with low phase-randomness [19] such as the present study, which concentrates on a close-spacing configuration having strong phase locking on the large coherent structures. The ensemble-averaging mode on the instantaneous velocity fields eliminates the fluctuations due to incoherent unsteadiness that are associated with turbulence (resolving small scales was not an objective of this study) and still permits a comparison with CFD predictions. Statistical filtering was also performed employing routines that allow removal of outliers from the data using standard-deviation trimming and other techniques [6,20].

Many factors are involved in the instantaneous-PIV uncertainty-calculation process (e.g., laser, CCD, seeding, imaging, algorithms, photodiode, and oscilloscope). The highest uncertainty was found to be associated with the velocity calculation that involves Δx (the displacement in pixels of each interrogation region), Δt (the time interval between the two exposures), and the magnification of the digital image relative to the object (pixel/m). The displacement in pixels obtained by peak-locator algorithms can provide subpixel accuracy (<0.1 pixels) after correction for various biases [4]. The Δt was adjusted to yield typical displacements of the main stream of >10 pixels; the uncertainty is, thus, $<1\%$. Values in the wake region, however, may have higher uncertainties due to the lower Δx. The maximum uncertainty in Δt was calculated from the time interval between the two laser light pulses with the aid of a photodiode that was connected to an oscilloscope (uncertainty 2%). It was found that this uncertainty increases with lower laser power and with lower Δt. A conservative uncertainty for the present experiments, which employed a Δt of about 1–2 μs and powers of around 10–20 mJ, was found to be 1%. The magnification was measured, using images of grids located in the laser-sheet plane, to better than 1%. Combining these conservative measurements of uncertainty yields a maximum error of $<2\%$ in the freestream velocity and $\sim 10\%$ in the wake velocity near the WG area.

The uncertainty that results from various PIV algorithms (e.g., single pass and multipass) and data-filtering techniques (e.g., standard-deviation trimming and median) was also calculated for the average velocity field. Mean, standard deviation, median, and median variability were calculated for the data sets and compared for each PIV algorithm and filtering technique. The average velocity field was interrogated at the various representative regions such as the freestreams above and below the WG and before and after the shock, the shock regions, and the wake regions. The median variability was calculated using the "median absolute deviation" (MAD), which is defined as the median of the absolute distances to the median and is computed as an alternative to the standard deviation when that is not available. That was the case in the present experiments with sample sizes of 50 elements, which effectively allowed the computing of only one median. Therefore, its uncertainty, variability, and standard deviation cannot be calculated from a large-series standpoint, which would require a large population of medians. MAD is a robust measure of the median dispersion and does not have restrictions on the underlying distribution (such as normality). The mean uncertainty for Gaussian distributions is reduced by a factor of $1/\sqrt{N}$ (with N being the number of realizations) with respect to the uncertainty of the instantaneous values. If the sample size is low (<30), a t-distribution test is more adequate to measure confidence [20]. The results showed that, with proper multipass PIV algorithms and data-filtering techniques, the mean standard deviation and the median variability could be decreased to $<2\%$ and $<1\%$, respectively, with the median offering more uniform and consistently lower variability in all areas. In the wake region these values increased to $<12\%$ and $<10\%$, respectively, which could be attributed in part to actual phase-randomness [19].

Results

At 100% speed, consecutive rotor blades are separated in time by 140 μs ($\sim$11 deg in angle, the blade-row pitch). Seven blade locations ("clockings") separated by 20 μs were chosen to characterize the flowfield in a blade-row pitch. Analyses were performed using both qualitative flow-visualization and quantitative velocity-field measurements. Data analysis includes inspection and selection of flow-visualization images (obtained by increasing the amount of seeding) and also reduction of data to velocity using PIV software [17].

Previous research on this test article [6] demonstrated the effect of changing the axial spacing on the synchronization between vortex shedding and the rotor LE; the influence and synchronization between the blade passage and the flow was shown to decrease with increasing axial spacing. It became evident that close spacing offers stronger phase-locked flow features. The present experiments were focused on the "close-spacing-and-75%-span" configuration for studying the effect of the compressor operating point on the vortex-shedding pattern. The various operating conditions were achieved by changing the throttle settings (000, open throttle; 114, peak efficiency; 128; 135; and 140, near stall; see Fig. 3). Figure 6 shows flow-visualization samples for four throttle settings and two blade clockings that capture the passage of the rotor blade behind the WG. The figure shows the effect of throttle variation (000, open throttle; 114, peak efficiency; 128; and 140, near stall) on vortex shedding at two instants of blade passage behind the WG (140 μs, top, and 20 μs, bottom); dashed lines connecting the two vortex centers are shown to aid in visualizing their location. It can be readily inferred from these visualizations that vortex shedding from the WG displays a distinct pattern for each throttle condition. The vortices appear farther upstream as the throttle is closed to near stall (140), as opposed to when it is open (000). Increasing backpressure moves the bow-shock upstream, thus causing vortices to be shed sooner for the same rotor location. For the conditions of open throttle (000) and peak efficiency (114), a vortex appears to collide with the LE of the rotor blade, although at peak efficiency the vortex appears at a location of slightly higher pitch. When the throttle is closed to the

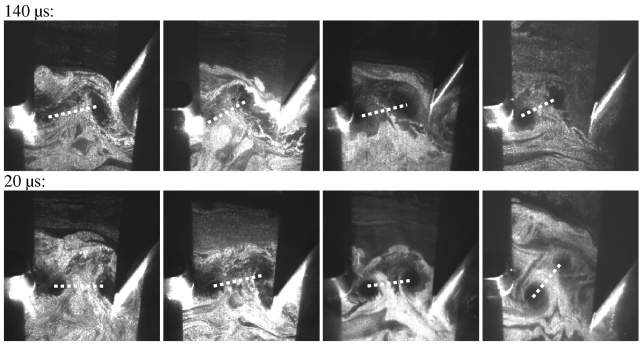

Fig. 6 Flow-visualization samples showing the effect of throttle variation on vortex shedding.

near-stall operating condition (140), the rotor appears to chop the wake by the "braid" (the region of the wake between the coherent structures) [19]. The rotor-blade LE location at a given clocking does not coincide exactly with those for different throttle settings because the mechanical speed was varied during the experiments to maintain the same corrected speed.

As observed in previous studies [6], synchronization of the rotor-blade location and vortex shedding was apparent upon inspection of the many images captured under various blade-delay and throttle conditions. This study demonstrates that the synchronization is evident at all operating points between choke and stall. The images of vortex shedding were similar for any given operating condition and blade delay. These facts have suggested that the location of the vortices (and shedding) is phase locked to the rotor-blade pass frequency. Further studies of the relation among blade-row axial spacing, vortex shedding, and compressor–rotor performance can be found in the literature [3,6,23]. Other studies of the relation between the frequency of the vortex shedding and the blade-passing frequency in a multiblade row of a turbine stage can also be found in the literature [24,25].

In the present experiments the rotor-blade row appears to produce forcing of the vortex shedding that is sufficiently strong [19] to cause sharp synchronization between the rotor-blade position and the main flow features. Forced shedding is triggered by the rotor-blade potential field, which transmits a strong pressure perturbation to the WG. A pressure fluctuation translates to a velocity perturbation as it interacts with the solid surface of the WG. The location of the interaction determines the characteristics of the vortex shedding. Also, because the bow shock is a major cause of pressure change and because the shock location with respect to the rotor LE varies with throttle setting, the difference in the location of the vortices as a function of the throttle setting is related to the shock location. This is consistent with WG the results of surface-static-pressure measurements made using Kulite transducers, which showed a strong fluctuation in pressure at the blade-passing frequency [26]. Furthermore, a recent cascade experiment confirmed that large vortices can be induced by the passing of a shock wave [27].

An improved quantitative understanding of the many unsteady-flow features involved in complex blade-row interactions can be gained through analysis of the velocity field obtained with PIV. As pointed out earlier, because vortex shedding is phase locked to rotor passage, rotor phase-locked averaging is possible without destruction of the main details of the velocity field in this interaction region. Also, in the instantaneous-PIV data, gaps in the velocity information may be present where seeding was not sufficient to obtain a correlation; thus, more reliable information can be gained by considering the average flowfield where data intermittency can be minimized. In a phase-locked flow with strong statistical central tendencies of the events under study, the median is both an advantageous estimator of the central value and a robust statistic for removal of outliers, as explained in the PIV section.

The velocity field provides evidence of the relationship among vortex shedding, shock position, wake–shock interaction, and operating condition. Quantitative information on the actual location of the vortices and the shock with respect to the WG and rotor blade can be easily obtained.

Figure 7 shows the PIV velocity field (median of 50 files) overlaid with streamtraces for the choke (open throttle, 000) operating condition at three blade clockings that represent the rotor blade passage behind the WG. The rotor-bow shock, clearly discernible as an abrupt change in velocity, is at a constant distance from the rotor but is broken by the shed wake, which is clearly discernible as a low-velocity region. A significant pitchwise motion of the wake, defined by the shed vortices, was observed as it advected downstream (and also as a function of the rotor-blade location).

The velocity field for the blade clocking with the rotor LE aligned at the WG TE is presented in Fig. 8 (median of 50 files) for three throttle conditions. The rotor-bow shock can be easily identified for each operating condition. Between open throttle (000) and peak efficiency (114), the bow shock begins to move forward as the stage becomes unchoked and the backpressure increases. Furthermore,

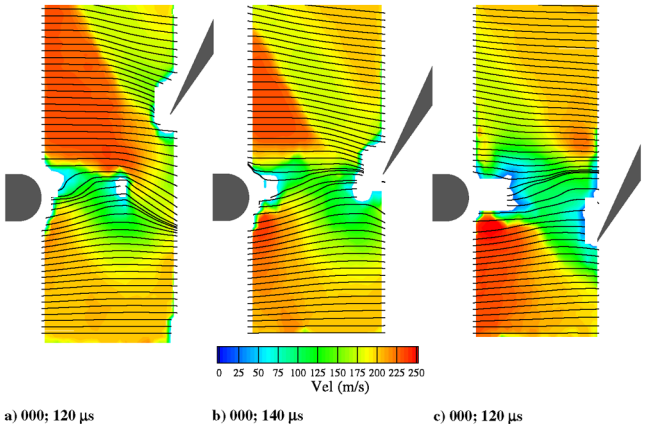

Fig. 7 Velocity field and streamtraces for open throttle condition at three blade clockings.

until the stage becomes completely unchoked, the mass flow rate is constant, as shown by the characteristic of Fig. 3. Thus, the velocity in the PIV image of Fig. 8a is similar to that of Fig. 7b. At near stall (where the shock is farther upstream for a given blade clocking), the vortex that is colliding with the rotor LE is actually shed from a previous rotor-blade-bow shock. As the throttle goes from open (000) to near stall (140), the rotor-bow shock becomes stronger and moves upstream, which causes the greatest changes in velocity magnitude and flow angle across the shock. The PIV image shows mainly the flow features upstream of the rotor blade and above the rotor suction side, but some figures (Figs. 7c and 8c) provide evidence of the pressure-side LE shock just below the rotor blade. At the peak-efficiency operating condition, the pressure-side shock is more normal to the rotor LE and, therefore, can be observed in the image view.

An approximation of the overall time-averaged velocity field can be obtained by averaging all seven blade delays of one blade passing behind the WG. Figure 9 shows the velocity field (median of the seven blade clockings with 50 files each) and the corresponding streamtraces for a blade-passage period behind the WG for three throttle conditions: a) peak efficiency, 114; b) 128; and c) near stall, 140. At peak efficiency, the magnitude of the velocity is high above and below the wake and rotor incidence is nearly zero. As the throttle is closed to near stall, the magnitude of the velocity is decreased significantly, and the flow enters the rotor at a negative angle. Further analyses of the velocity field yield details on the shock magnitude and location. The abrupt velocity change through the shock can be analyzed using line plots of velocity magnitude across the shock. Figure 10 shows three axial profiles of average speed (median) through the shock for the peak-efficiency case where the rotor LE is located at 10% WG pitch above the WG center (corresponding to a

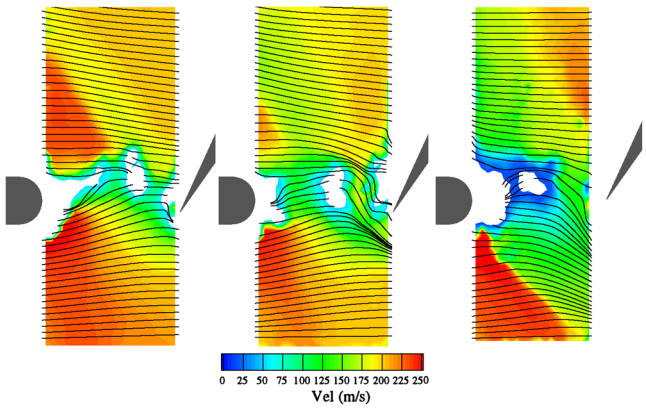

Fig. 8 Velocity field and streamtraces for a blade clocking at three throttle conditions.

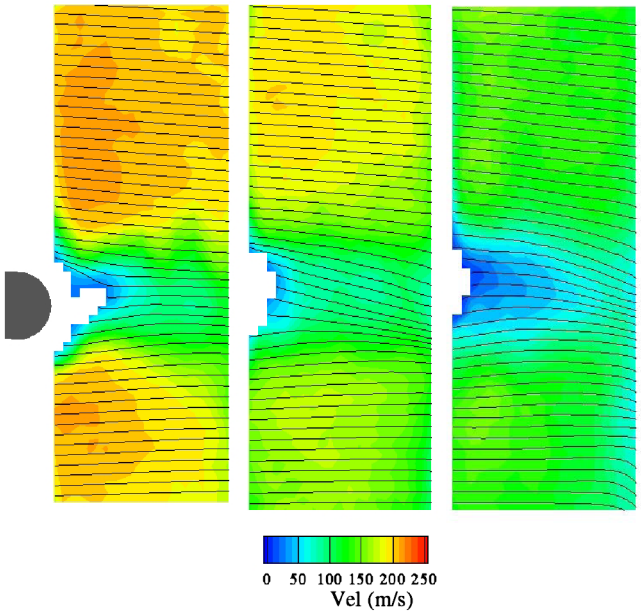

Fig. 9 Velocity field and streamtraces for a blade period at three throttle conditions.

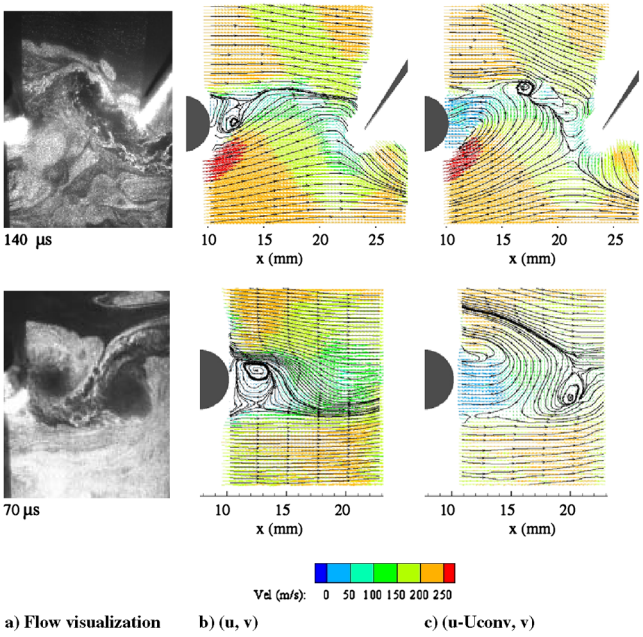

Fig. 11 Wake motion and wake–shock interaction characterizations at peak efficiency.

clocking of 120 μs). Here the resolution of the PIV was 32 pixel cells with 75% overlap that produce an 8 pixel (0.2925 mm) grid (shown in the figure). The shock is readily discernible far from the wake at 20 and 15% WG pitch above the WG center, but it widens and weakens close to the wake, such as at 10% pitch. The width of the bow shock is smeared by PIV resolution. Higher-resolution measurements or close-up approaches [28] would be required for more accurate determination of the actual shock location and velocity gradient, provided the seeding was appropriate [4]. However, the velocity jump across the shock can be readily estimated, for example, $235 - 181.5 = 53.5$ m/s for the case of 20% pitch above the WG. Also the shock location can be estimated from the curve where the speed changes rapidly. For example, here the center could be estimated to be at $\sim$12.5 mm (12.5 ± 0.5 mm) or 22.5% chord upstream of the rotor LE. The shock width and sharpness are readily discernible far from the wake at 15 and 25% WG pitch above the WG center but become smeared near the wake region (e.g., 10% WG pitch above the WG center) because of the wake–shock interaction. Moreover, because the velocities across the shock wave can be calculated in the rotor frame of reference, the Mach number of the shock could be calculated and compared with the value from the known blade and flow velocities or shock angle.

The large vortices that appear in the wake flow can significantly influence the flow entering the rotor. These features are also important for validating time-accurate CFD codes. The complex flowfield accompanying the shock, vortices, and wake can be investigated through additional processing of the PIV velocity data. Capturing higher levels of detail in these areas was accomplished using multipass high-resolution PIV with an increased grid resolution of 0.292 mm and various averaging filters that are explained in the PIV section. Figure 11 shows the manner in which these details can be obtained by subtracting a constant axial component (convective) of velocity to represent the motion from a frame of reference moving at that velocity [29]. Results at blade clockings of 70 μs (wake passing through the center of rotor passage) and 140 μs (rotor LE aligned with WG) for peak efficiency are shown to emphasize the wake motions. The wake vortices and the braid can be clearly seen in the instantaneous flow visualizations in Fig. 11a. Topological wake features can be identified from the streamline patterns; the first vortex shed (spiraling streamline pattern), the saddle points (outward-pointing streamline pattern from a center), and the strong downwash velocity between the vortices through the braid (in the 70-μs clocking) are clearly discernible from the mean velocity field and streamtraces (Fig. 11b). These motions occur close to the nearly quiescent region behind the WG, and convective velocity subtraction is not needed. Further insight regarding the interaction of the rotor-bow shock with the WG TE can be gained from PIV and flow-visualization data. In Fig. 11b, a shed vortex appears on the upper side (facing rotor revolution) of the WG, which suggests that the rotor-bow shock influences the WG boundary layer in a manner that drives the shedding of a vortex. The nature of the perturbation that drives vortex shedding has been described in the literature [3] through a comparison of the results of detailed experimental measurements with time-accurate CFD simulations. The second vortex and saddle point can also be readily identified when their convective velocity (obtained from the absolute velocity field, here $\sim$110 m/s) is subtracted from the mean (Fig. 11c). A shock–vortex interaction is captured for the second vortex at 140 μs, as shown in Fig. 11c, which depicts the location of the vortex in the middle of the shock line.

Other details of the flow can be obtained by smoothing (weighted average of neighboring points) the velocity field. This technique emphasizes flow patterns that can be used for time-accurate CFD comparisons. Such a wake characterization is shown for the 70-μs clocking in Fig. 12. The first (Fig. 12a) and second (Fig. 12b) vortices and the saddle points from Fig. 11 are readily discernible with their characteristic patterns. The wake profiles and wake centerline (Fig. 13) also provide evidence of the wake motions, waviness, and

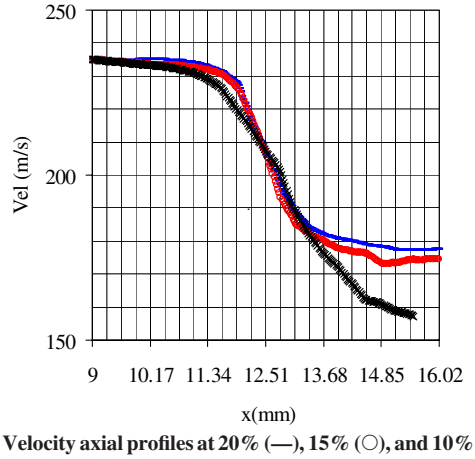

Fig. 10 Velocity axial profiles at 20% (—), 15% (○), and 10% (x) pitch.

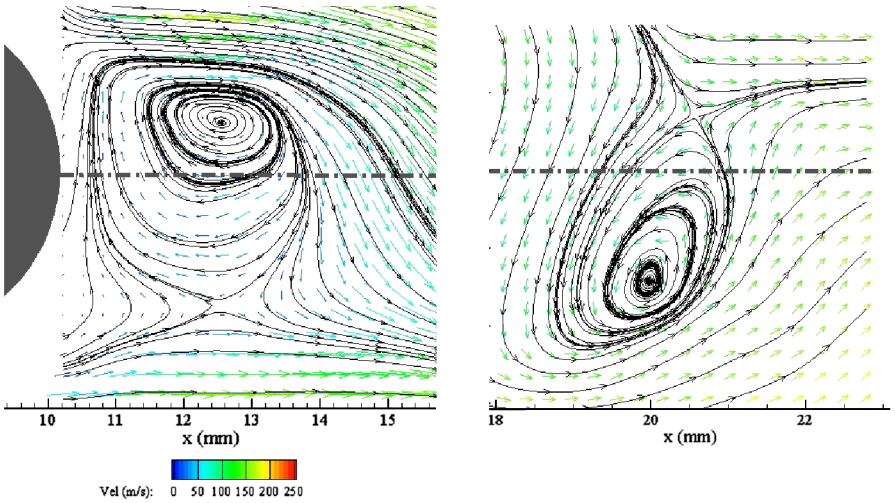

a) First vortex b) Second vortex

Fig. 12 Details of the wake displayed through smoothed vector field; WG axial centerline (dash-dotted lines).

reduction in incidence at the raw exit. The centerline was defined by joining the minima of the velocity profiles. Comparison of the averaged wakes over a period has proved to be very useful [30].

Conclusions

The flowfield between an upstream stator and a downstream rotor closely spaced in a high-speed highly loaded transonic compressor was investigated using flow-visualization and PIV measurements at various operating conditions. A distinct vortex-shedding and shock pattern was documented for several throttle positions from choke to stall. Because vortex shedding from the WG is strongly synchronized with the passage of the rotor-bow shock at close spacing, phase-locked measurements allow multiple images of any blade position to be averaged, producing a clear image of the flowfield. This study demonstrates that the vortex shedding is synchronized to the passage of the rotor-bow shock at all operating conditions from choke to stall. As the operating point changes from choke to stall and the rotor-bow shock moves upstream, the spatial relation between the rotor blade and shed vortex is modified. Thus the rotor LE may collide with a vortex or chop the wake by the braid, depending on the throttle position. The velocity fields exhibit the motion of the wake including shed vortices as well as the changes in velocity magnitude and flow angle across the shock for each compressor operating condition. For each condition, PIV images present evidence of the shock location, velocity magnitude, and details of its interaction with the wake and vortex shedding. An average velocity field defined by seven positions in one rotor-blade period revealed that the incidence increased as the operating condition changed from peak efficiency to near stall.

Analysis of the PIV data has been used to provide insight into vortex shedding, rotor-bow-shock location, and wake–shock interaction. Through the use of data-processing techniques such as multipass high-resolution PIV with statistical data filtering and averaging, convective velocity subtraction, and smooth-weighted averaging, it has been demonstrated that the complex unsteady flowfield can be captured and visualized with great detail and clarity, allowing previously undetected unsteady-flow phenomena to be observed. These methods have proved useful for isolating specific shed vortices and the shock–vortex interaction in this advanced transonic compressor. Additionally, the data presented allows verification and validation of time-accurate CFD codes.

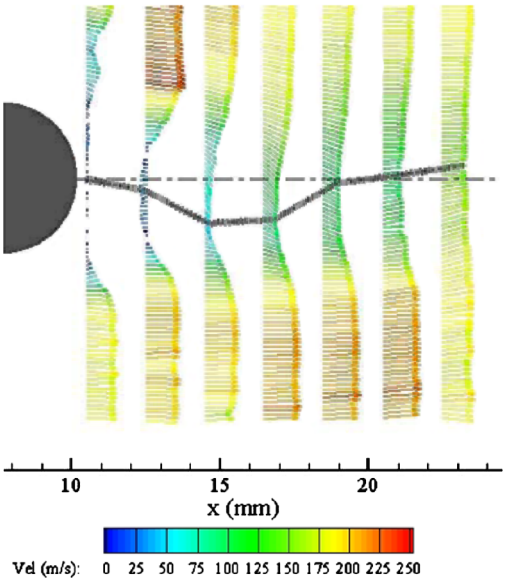

Fig. 13 Wake profiles and centerline waviness: wake characterization example at 70-μs clocking.

Acknowledgments

The authors acknowledge the technical assistance of personnel at Compressor Aerodynamics Research Laboratory (CARL), Wright–Patterson Air Force Base, OH, and at Innovative Scientific Solutions, Inc. (ISSI), during the experiments and the editorial assistance of Marian Whitaker of ISSI. The WG, rotor, and stator were built by Pratt & Whitney. The authors recognize Robert Wirrig, Ron Berger, and Terry Norris from the CARL group at Wright–Patterson Air Force Base, OH, for their assistance in gathering the data. Justin England and Nathan Woods assisted with postprocessing of the results. The authors acknowledge the Propulsion Directorate management for supporting the research and the presentation and publication of this paper. Very fruitful discussions with Josep Ginebra, Professor of Statistics at the Polytechnic University of Catalonia, are greatly appreciated.

References

[1] Adamczyk, J. J., "Aerodynamic Analysis of Multistage Turbomachinery Flows in Support of Aerodynamic Design," *Journal of Turbomachinery*, Vol. 122, No. 2, 2000, pp. 189–217.

[2] Gorrell, S. E., Okiishi, T. H., and Copenhaver, W. W., "Stator Rotor Interactions in a Transonic Compressor, Part 2: Description of a Loss Producing Mechanism," *Journal of Turbomachinery*, Vol. 125, No. 2, Apr. 2003, pp. 328–335.

[3] Gorrell, S. E., Car, D., Puterbaugh, S. L., Estevadeordal, J., and Okiishi, T. H., "An Investigation of Wake-Shock Interactions in a Transonic

Compressor with DPIV and Time-Accurate CFD," *Journal of Turbomachinery*, Vol. 128, Oct. 2006, pp. 616–626; also *Proceedings of the ASME Turbo Expo*, American Society of Mechanical Engineers Paper GT-2005-69107, June 2005.

[4] Raffel, M., Willert, C. E., and Kompenhans, J., *Particle Image Velocimetry: A Practical Guide*, Springer–Verlag, New York, 1998.

[5] Copenhaver, W., Estevadeordal, J., Gogineni, S., Gorrell, S., and Goss, L., "DPIV Study of Near-Stall Wake-Rotor Interactions in a Transonic Compressor," *Experiments in Fluids*, Vol. 33, No. 6, 2002, pp. 899–908.

[6] Estevadeordal, J., Gogineni, S., Goss, L., Copenhaver, W., and Gorrell, S., "Study of Wake-Blade Interactions in a Transonic Compressor Using Flow Visualization and DPIV," *Journal of Fluids Engineering*, Vol. 124, No. 1, 2002, pp. 166–175.

[7] Estevadeordal, J., Gogineni, S., Goss, L., Copenhaver, W., and Gorrell, S., "DPIV Study of Wake-Rotor Synchronization in a Transonic Compressor," AIAA Paper 2001-3095, June 2001.

[8] Estevadeordal, J., Gogineni, S., Copenhaver, W., Bloch, G., and Brendel, M., "Flow Field in a Low-Speed Axial Fan: A DPIV Investigation," *Experimental Thermal and Fluid Science*, Vol. 23, Nos. 1–2, 2000, pp. 11–21.

[9] Wernet, M. P., "Development of Digital Particle Imaging Velocimetry for Use in Turbomachinery," *Experiments in Fluids*, Vol. 28, No. 2, 2000, pp. 97–115.

[10] Balzani, N., Scarano, F., Riethmuller, M. L., and Breugelmans, F. A. E., "Experimental Investigation of the Blade-to-Blade Flow in a Compressor Rotor by Digital Particle Image Velocimetry," *Journal of Turbomachinery*, Vol. 122, No. 4, 2000, pp. 743–750.

[11] Sanders, A. J., Papalia, J., and Fleeter, S., "A PIV Investigation of Rotor-IGV Interactions in a Transonic Compressor," *Journal of Propulsion and Power*, Vol. 18, No. 5, Sept.–Oct. 2002, pp. 969–977.

[12] Law, C. H., and Wennerstrom, A. J., "Two Axial Compressor Designs for a Stage Matching Investigation," U.S. Air Force Wright Aeronautical Laboratories Rept. AFWAL-TR-89-2005, Wright–Patterson AFB, OH, 1989.

[13] Gorrell, S., Copenhaver, W., and Chriss, R., "Upstream Wake Influences on the Measured Performance of a Transonic Compressor Stage," *Journal of Propulsion and Power*, Vol. 17, No. 1, 2001, pp. 43–48.

[14] Creason, T., and Baghdadi, S., "Design and Test of a Low Aspect Ratio Fan Stage," AIAA Paper 88-2816, July 1988.

[15] Schlichting, H., *Boundary-Layer Theory*, McGraw–Hill, New York, 1979.

[16] Hecht, E., *Optics*, Addison Wesley Longman, Reading, MA, 1990.

[17] DPIV Software, Innovative Scientific Solutions, Inc., Dayton, OH, 2001.

[18] Hart, D. P., "Super-Resolution PIV by Recursive Local-Correlation," *Journal of Visualization*, Vol. 3, No. 2, Sept. 2000, pp. 187–194.

[19] Estevadeordal, J., and Kleis, S., "High-Resolution Measurements of Two-Dimensional Instabilities and Turbulence Transition in Plane Mixing Layers," *Experiments in Fluids*, Vol. 27, No. 4, 1999, pp. 378–390.

[20] Coleman, H. W., and Steele, W. G., *Experimentation and Uncertainty Analysis for Engineers*, Wiley, New York, 1989.

[21] Inoue, L. Y. T., Berry, D. A., and Parmigiani, G., "Relationship Between Bayesian and Frequentist Sample Size Determination," *American Statistician*, Vol. 59, No. 9, Feb. 2005, p. 79.

[22] Press, W. H., Flannery, B. P., Teukolsky, S. A., and Vetterling, W. T., *Numerical Recipes in C: The Art of Scientific Computing*, Cambridge Univ. Press, New York, 1992.

[23] Zachcial, A., and Nurnberger, D., "A Numerical Study on the Influence of Vane-Blade Spacing on a Compressor Stage at Sub- and Transonic-Operating Conditions," *ASME Turbo Expo: Power for Land, Sea, and Air*, American Society of Mechanical Engineers Paper GT-2003-38020, 2003.

[24] Sondak, D. L., and Dorney, D. J., "Simulation of Vortex Shedding in a Turbine Stage," *Journal of Turbomachinery*, Vol. 121, No. 3, 1999, pp. 428–435.

[25] Woisetschlager, J., Mayrhofer, N., Hampel, B., Lang, H., and Sanz, W., "Laser-Optical Investigation of Turbine Wake Flow," *Experiments in Fluids*, Vol. 34, No. 3, 2003, pp. 371–378.

[26] Koch, P., Probasco, D., Wolff, M., Copenhaver, W., and Chriss, R., "Transonic Compressor Influences on Upstream Surface Pressures with Axial Spacing," *International Gas and Aeroengine Congress and Exhibition*, American Society of Mechanical Engineers Paper 99-GT-384, June 1999.

[27] Langford, M., Guillot, S., Ng, W., Breeze-Stringfellow, A., Solomon, W., and Estevadeordal, J., "Experimental Investigation of the Effects of a Moving Shock Wave on Compressor Stator Flow," *ASME Turbo Expo: Power for Land, Sea, and Air*, American Society of Mechanical Engineers Paper GT-2005-68722, 2005; also *Journal of Turbomachinery* (to be published).

[28] Estevadeordal, J., Copenhaver, W., Car, D., Koch, P., Ng, W., Guillot, S., and Carter, C., "Macro- and Milli-DPIV Studies of a Boundary-Layer-Based Flow-Control System for a Transonic Cascade," *Proceedings of the 11th International Symposium on Application of Laser Techniques to Fluid Mechanics* [CD-ROM], 2002.

[29] Adrian, R. J., Christensen, K. T., and Liu, Z.-C., "Analysis and Interpretation of Instantaneous Turbulent Velocity Fields," *Experiments in Fluids*, Vol. 29, No. 3, 2000, pp. 275–290.

[30] Gorrell, S., Copenhaver, W., and Estevadeordal, J., "DPIV Measurements of the Flow Field Between a Transonic Rotor and an Upstream Stator," *Proceedings of the International Symposium on Unsteady Aerodynamics, Aeroacoustics, Aeroelasticity of Turbomachines (ISUAAAT)*, Kluwer Academic, Norwell, MA, 2003, pp. 505–520.

L. Xu
Associate Editor